UNLV | **University Libraries**
University of Nevada, Las Vegas

Geoscience Faculty Publications

Geoscience

2-27-2020

Thermal Analysis, Compressibility, and Decomposition of Synthetic Bastnäsite-(La) to Lanthanum Oxyfluoride

Richard L. Rowland
Los Alamos National Laboratory, rlrowland@lanl.gov

Barbara Lavina
University of Nevada, Las Vegas

Kathleen E. Vander Kadeen
NASA Johnson Space Center, Kathleen.E.VanderKaaden@NASA.Gov

Lisa R. Danielson
Los Alamos National Laboratory, LDanielson@LANL.Gov

Pamela C. Burnely
University of Nevada, Las Vegas, pamela.burnley@unlv.edu

Follow this and additional works at: https://digitalscholarship.unlv.edu/geo_fac_articles

Part of the Geochemistry Commons, and the Geophysics and Seismology Commons

Thermal Analysis, Compressibility, and Decomposition of Synthetic Bastnäsite-(La) to Lanthanum Oxyfluoride

Richard L. Rowland II [1,*], Barbara Lavina [2,†], Kathleen E. Vander Kaaden [3], Lisa R. Danielson [4] and Pamela C. Burnley [5,*]

[1] Static High Pressure Team, Explosive Science and Shock Physics (M-9), Los Alamos National Laboratory, Los Alamos, NM 87544, USA

[2] High Pressure Science and Engineering Center, University of Nevada Las Vegas, Las Vegas, NV 89154, USA; Blavina@anl.gov

[3] Astromaterials Research and Exploration Science Division (ARES), Jacobs, NASA Johnson Space Center, Mail Code XI3, Houston, TX 77058, USA; Kathleen.E.VanderKaaden@NASA.Gov

[4] Space and Remote Sensing (ISR-2), Los Alamos National Laboratory, Los Alamos, NM 87544, USA; LDanielson@LANL.Gov

[5] High Pressure Science and Engineering Center and Geoscience Department, University of Nevada Las Vegas, Las Vegas, NV 89154, USA

* Correspondence: rlrowland@lanl.gov (R.L.R.II), Pamela.Burnley@unlv.edu (P.C.B.)

† Current affiliation: X-ray Science Division, Argonne National Laboratory, Argonne, Illinois 60439, USA.

Abstract: Understanding basic material properties of rare earth element (REE) bearing minerals such as their phase stability and equations of state can assist in understanding how economically viable deposits might form. Bastnäsite is the most commonly mined REE bearing mineral. We synthesized the lanthanum-fluoride end member, bastnäsite-(La) ($LaCO_3F$), and investigated its thermal behavior and decomposition products from 298 K to 1173 K under ambient pressure conditions through thermogravimetric analysis, differential scanning calorimetry, evolved gas analysis, and high temperature powder X-ray diffraction. We also investigated the compressibility of bastnäsite-(La) via single crystal X-ray diffraction in diamond anvil cells at an ambient temperature up to 11.3 GPa and from 4.9 GPa to 7.7 GPa up to 673 K. At ambient pressure, bastnäsite-(La) was stable up to 598 K in air, where it decomposed into CO_2 and tetragonal γ-LaOF. Above 948 K, cubic α-LaOF is stable. High temperature X-ray diffraction data were used to fit the Fei thermal equation of state and the thermal expansion coefficient α_{298} for all three materials. Bastnäsite-(La) was fit from 298 K to 723 K with $V_0 = 439.82$ Å³, $\alpha_{298} = 4.32 \times 10^{-5}$ K⁻¹, $a_0 = -1.68 \times 10^{-5}$ K⁻¹, $a_1 = 8.34 \times 10^{-8}$ K⁻¹, and $a_2 = 3.126$ K⁻¹. Tetragonal γ-LaOF was fit from 723 K to 948 K with $V_0 = 96.51$ Å³, $\alpha_{298} = 2.95 \times 10^{-4}$ K⁻¹, $a_0 = -2.41 \times 10^{-5}$ K⁻¹, $a_1 = 2.42 \times 10^{-7}$ K⁻¹, and $a_2 = 41.147$ K⁻¹. Cubic α-LaOF was fit from 973 K to 1123 K with $V_0 = 190.71$ Å³, $\alpha_{298} = -1.12 \times 10^{-5}$ K⁻¹, $a_0 = 2.36 \times 10^{-4}$ K⁻¹, $a_1 = -1.73 \times 10^{-7}$ K⁻¹, and $a_2 = -17.362$ K⁻¹. An ambient temperature third order Birch–Murnaghan equation of state was fit with $V_0 = 439.82$ Å³, $K_0 = 105$ GPa, and $K' = 5.58$.

Keywords: Bastnäsite; equation of state; rare earth element

1. Introduction

Rare earth elements (REE), the elements with atomic number 57 to 71, are the first on the periodic table to begin populating F-block orbitals. Due to this fact, they exhibit unique electronic properties and thus are sought after for various technological applications for which other metals are not suitable. They are considered rare, not because of their relative abundance in the Earth's crust, but

because they are generally only found as trace impurities instead of primary cations in minerals [1,2]. Relative crustal abundances of REEs are higher than noble metals such as gold or platinum, and some REEs are more common than base metals like lead [2,3]. The limited number of minerals that form with high REE content are rarely found in high enough concentrations to make economically viable deposits [2]. Currently, China controls > 90% of the world's supply of REEs [1], presenting the potential for a supply problem. Understanding basic material properties of REE bearing minerals such as how they respond to changes in pressure and temperature can assist in understanding how economically viable deposits form.

Having the general formula of $(Ce,La,Nd,Y)CO_3(F,OH)$, bastnäsite is the most common mineral mined for REEs [4]. It occurs mainly in carbonatites and is usually found in association with calcite, dolomite, and barite [5–7], but also occurs in other geologic settings important for REE-bearing minerals [8]. Bastnäsite-(La) is the lanthanum fluoride end member $(LaCO_3F)$ [2,4,9–14]. This work explores the ambient pressure thermal behavior of bastnäsite-(La) and the oxyfluorides it decomposes to using thermogravimetric analysis, differential scanning calorimetry, evolved gas analysis, and high temperature X-ray powder diffraction. We also explore the behavior of bastnäsite-(La) at high pressure via single crystal X-ray diffraction in a diamond anvil cell.

1.1. Structure and Decomposition of Bastnäsite-(La) to Lanthanum Oxyfluoride

Bastnäsite-(La) $(LaCO_3F)$ exhibits hexagonal symmetry in the P-62c space group. Each unit cell contains six formula units of alternating layers of carbonate anions and layers of lanthanum cations and fluorine anions (Figure 1). The lanthanum-fluoride layers are parallel to the *a*- axis while the carbonate anion groups between them are locally parallel to the *c*- axis [4,9,10]. With the application of sufficient energy in the form of heat, bastnäsite-(La) decomposes via the decarbonation reaction $LaCO_3F + (heat) = LaOF + CO_2$ [7,15]. At ambient conditions, γ-LaOF exhibits tetragonal symmetry in the P4/nmm space group with two formula units per unit cell [16–20]. At high temperature, α-LaOF is stable with cubic symmetry in the Fm-3m space group with four formula units per unit cell [21–25]. β-LaOF is reported as stable at ambient pressure and temperature exhibiting rhombohedral symmetry in the R-3m space group with six formula units per unit cell [16,20,24]. This structure was not encountered during this investigation.
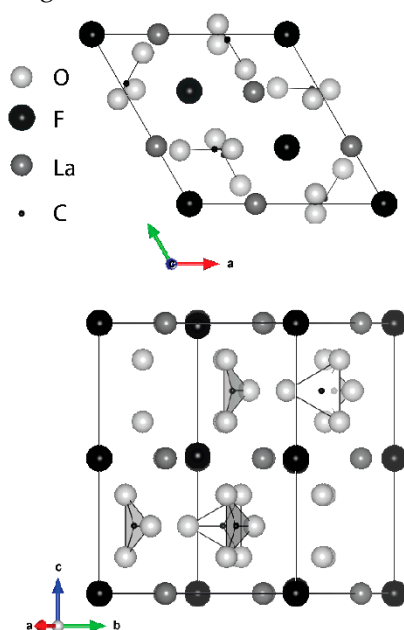
Figure 1. Structure of bastnäsite-(La) generated in the software VESTA [26], (**a**) as viewed down the *c*- axis, (**b**) as viewed down the *a**- axis [4]. In both images, the trigonal planar polyhedral for the CO_3^{2-} ions are highlighted.

2. Materials and Methods

2.1. Synthesis

Bastnäsite-(La) was synthesized via precipitation from an aqueous solution at room pressure and temperature using the method described by Janka and Schleid [15]. Aqueous solutions of each reagent were made by mixing powdered lanthanum nitrate ($La(NO_3)_3 \cdot 6H_2O$, Sigma Aldrich 203548-100G, > 99% purity), sodium bicarbonate ($NaHCO_3$, Sigma Aldrich S6014-25G, > 99% purity), and sodium fluoride (NaF, Sigma Aldrich 201154-5G, > 99% purity) with deionized water in separate beakers. The solutions were combined in a larger beaker. Bastnäsite-(La) precipitated from the mixture of solutions immediately, with sodium nitrate ($NaNO_3$) remaining in the solution. The fluid was decanted, and the bastnäsite-(La) precipitate was washed in deionized water and centrifuged to remove residual sodium nitrate. The powder was then dried in a Fischer Scientific model 289A Isotemp Vacuum oven under vacuum at 488 K for at least 12 h.

Phase identification was completed by powder X-ray diffraction in a PANalytical X'Pert PRO and photoaccoustic infrared spectroscopy on a Digilab FTS-7000 Fourier transfer infrared (FTIR) spectrometer. Rietveld structure refinement using X'pert Highscore Plus software was used to determine that the bastnäsite-(La) starting material contained < 10% LaF_3 impurity. No OH peaks were detected by FTIR between 3600 cm^{-1} and 3400 cm^{-1}.

The powder X-ray diffraction peaks from the synthesized bastnäsite-(La) are wide due to the small particle size, so the material was next annealed in a Griggs modified piston cylinder apparatus [27] using NaCl as the pressure transmitting medium. Samples were placed in a platinum jacket, surrounded by graphite, and sealed in a copper capsule, then subjected to pressures between 0.25 GPa and 1.0 GPa and temperatures from 973 K to 1123 K [28]. See Figure 2 for a comparison of diffraction patterns before and after annealing.
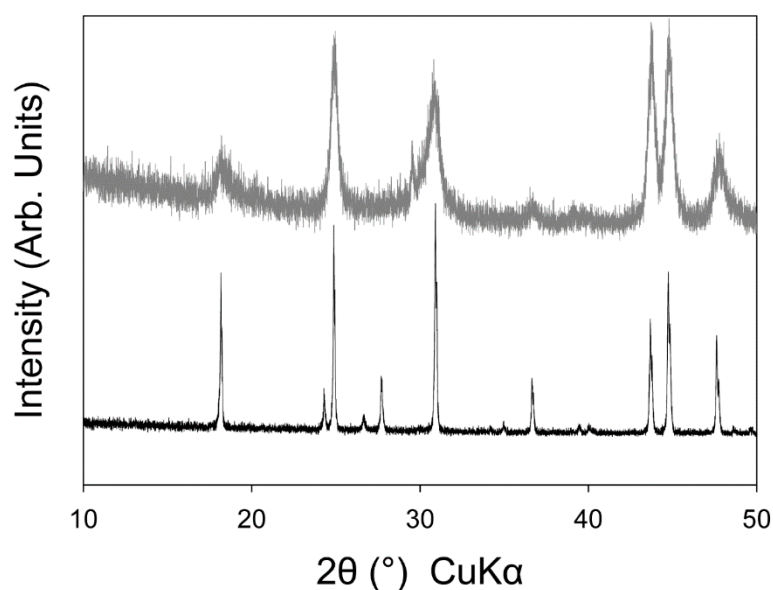
Figure 2. Powder XRD patterns of synthesized bastnäsite-(La) starting material. Top pattern is after washing and drying, bottom pattern is after annealing in the Griggs modified piston cylinder apparatus.

2.2. Themogravimetric Analysis and Differential Scanning Calorimetry

Thermogravimetric analysis (TGA), differential scanning calorimetry (DSC), and evolved gas analysis (EGA, Pfeiffer Vacuum Thermostar. Aßlar, Germany.) were used to determine the temperature at which bastnäsite-(La) begins to decompose and to determine the temperatures of phase transformations in the decomposition products. Powdered samples of at least 5 mg were heated in an alumina ceramic crucible in a Netzsch STA449 F1 Jupiter DSC/TGA apparatus under

dry N_2 at 1 atm pressure at a programmed rate of 5°/min from 313 K to 1223 K. Nitrogen was used as a carrier gas because it was unreactive with the sample during heating. A second empty alumina crucible was used as the reference. It is noted that the Netzsch Jupiter DSC/TGA apparatus contains a heat-flux style calorimeter, thus exothermic reactions produce a measured increase in heat flow. A Pfeiffer Vacuum Thermostar Quadrupole mass spectrometer was used to record select masses between 1–100 AMU throughout the temperature ramp.

2.3. High Temperature Powder X-Ray Diffraction

High temperature powder X-ray diffraction was used to determine unit cell volume as a function of temperature and to determine which phases were present at different temperatures. Measurements were made in air on a PANalytical X'Pert Pro MPD Diffractometer fitted with an Anton Paar XRK 900 thermal reactor stage and an X'celerator (2.02° 2θ) detector. A cobalt X-ray source (Co Kα_1 λ = 1.78901 Å) was used in angle dispersive mode from 4.0980 to 79.9814° 2θ with a step size of 0.0170° at 50.1650 s per step. Diffraction patterns were collected at 298 K, and in 50 degree increments from 323 K to 473 K, and in 25 degree increments from 473 K to 1173 K. A final pattern was collected at 298 K after the sample was allowed to cool. Data analysis was completed using QualX 2.0 [29], UnitCellWin64 [30] and EosFit7GUI [31].

### 2.4. Single Crystal X-Ray Diffraction

In situ single crystal synchrotron X-ray diffraction was performed at Sector 16 HPCAT of the Advanced Photon Source at Argonne National Laboratory. The pressure cells used were four-post diamond anvil cells (DAC) with 700 μm diameter culets and laser-cut rhenium gaskets with a 380 μm diameter laser-cut gasket hole sample chamber [32,33]. Single crystals of the annealed bastnäsite-(La) ~20 μm in diameter were placed in the sample chamber. Ruby spheres along with gold or copper powder were included in the sample chamber as pressure standards. The diamond cells were gas loaded [34] with helium, neon, or argon as the pressure transmitting media. Angle dispersive X-ray diffraction images were captured on a 2048 × 2048 pixel MAR CCD detector with a monochromatic beam of 30 keV energy X-rays (λ = 0.3738 nm) while rotating the DAC ±30 degrees around the vertical axis; allowing for between 50 and 300 bastnäsite-(La) reflections to be measured. The ruby luminescence pressure scale [35] was used to estimate pressure during data collection and the equations of state for gold [36] and copper [37] were used for final pressure determination. Heated DAC experiments were conducted in a vacuum chamber with kapton and mylar windows. The DAC was equipped with resistive heating wires wound around the gasket between the anvils and around the exterior of the DAC housing to generate and maintain sample chamber temperatures up to 673 K. Thermocouples were placed in contact with the diamonds to measure the sample temperature. For the heated experiments, argon was used as the pressure transmitting media, and copper (Cu) as the pressure standard. Data analysis was completed using the software packages Fit2D [38], MDI Jade (Materials Data Inc), GSE_ADA/RSV [39], and EosFit7GUI [31].

3. Results

3.1. Thermogravimetric Analysis and Differential Scanning Calorimetry

Thermogravimetric analysis and mass spectrometry CO_2 detection curves for annealed and unannealed bastnäsite-(La) and LaOF are displayed in Figure 3. Samples containing bastnäsite-(La) lost 1.0% to 1.3% between 313 K and 598 K due to adsorbed water. From 598 K to 778 K, 13.0% to 17.4% was lost due to the decomposition of bastnäsite-(La) to γ-LaOF and CO_2. Since the LaOF sample was generated by the decomposition of bastnäsite-(La), the minor deflection of its mass loss curve at the bastnäsite-(La) decomposition point is likely caused by minor amounts of remaining bastnäsite-(La). Otherwise, the curve for LaOF does not show a significant change in slope, indicating that the LaOF itself did decompose.

The differential scanning calorimetry curves for annealed and unannealed bastnäsite-(La) (Figure 4) exhibit endotherms between 598 K and 778 K, and the mass spectrometer's CO_2 detection peaked at 730 K. All samples exhibited exotherms at 948 K and endotherms at 1123 K, indicative of phase transitions.
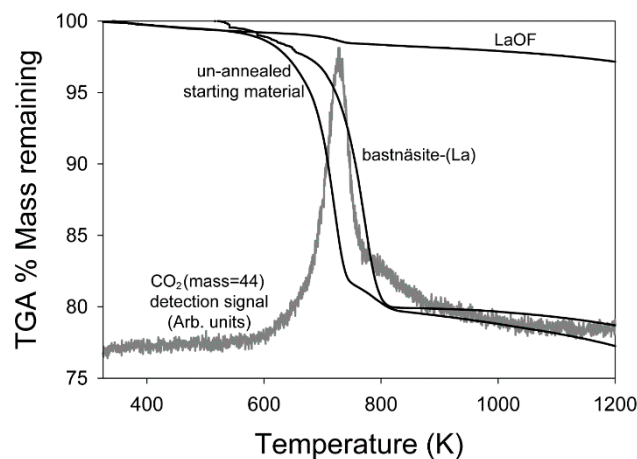
Figure 3. Thermogravimetric analysis (TGA) curves for annealed bastnäsite-(La), unannealed starting material, and LaOF from 325 K to 1223 K. CO_2 detection from the Pfeiffer Vacuum Thermostar Quadrupole mass spectrometer in light gray. Mass loss curves for the starting material and annealed bastnäsite-(La) begin to steepen at 600 K, at the same time CO_2 detection begins. The mass loss curve for LaOF does not show a significant change in slope, indicating that the decomposition reaction did not occur in that sample.
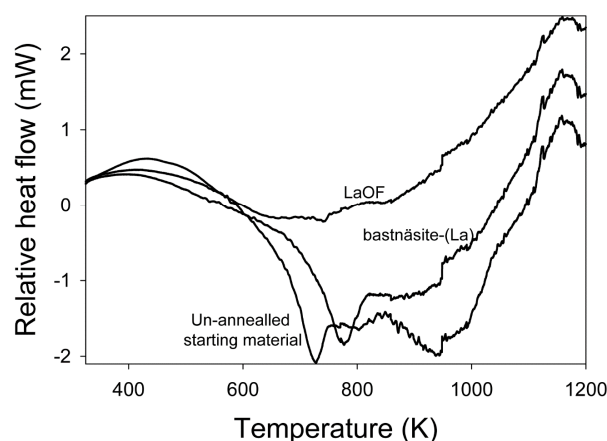
Figure 4. Differential scanning calorimetry (DSC) curves for annealed bastnäsite-(La), unannealed starting material, and LaOF from 325 K to 1223 K. Endotherms can be seen on both the annealed bastnäsite-(La), and unannealed starting material curves from the range near 598 K to 773 K, indicating the decomposition reaction. The LaOF curve does not exhibit this, since it did not decompose. Exotherms at 948 K and endotherms at 1123 K are evident on all three curves, indicating phase transformations.

3.2. High Temperature Powder X-Ray Diffraction

Figure 5 displays a selection of the high temperature powder XRD patterns encompassing the bastnäsite-(La) decomposition reaction. Bastnäsite-(La) is the dominant species in the X-ray diffraction patterns from 298 K to 723 K. Diffraction peaks for γ-LaOF begin to show up in the patterns above 598 K. By 773 K, bastnäsite-(La) is no longer present in the patterns, and γ-LaOF is the

only phase present. Above 948 K, only α-LaOF is present. γ-LaOF was the only species present in the pattern collected at 298 K after the sample was allowed to cool following the collection of the final high temperature pattern. β-LaOF was not evident in any of the patterns. See Tables 1–3 for the measured lattice parameters and volumes of all three materials. Figures 6–8 display measured unit cell volumes as a function of temperature for all three materials.

Table 1. Measured lattice parameters and volume for bastnäsite-(La) from 298 to 723 K.

| Temperature (K)	a (Å)	Uncertainty	c (Å)	Uncertainty	V (Å³)	Uncertainty	a/c ratio
298	7.1867	0.00085	9.8328	0.00083	439.82	0.185	0.7309
323	7.1897	0.00085	9.8347	0.00083	440.26	0.185	0.7311
373	7.1954	0.00085	9.8394	0.00083	441.18	0.185	0.7313
423	7.1992	0.00085	9.8438	0.00083	441.84	0.185	0.7313
473	7.2044	0.00085	9.8486	0.00083	442.69	0.186	0.7315
498	7.2074	0.00085	9.8504	0.00083	443.14	0.186	0.7317
523	7.2096	0.00085	9.8539	0.00083	443.57	0.186	0.7316
548	7.2125	0.00085	9.8564	0.00083	444.04	0.186	0.7318
573	7.2159	0.00085	9.8572	0.00083	444.50	0.186	0.7320
598	7.2172	0.00085	9.8598	0.00083	444.76	0.186	0.7320
623	7.2205	0.00086	9.8626	0.00083	445.30	0.186	0.7321
648	7.2238	0.00086	9.8669	0.00083	445.91	0.187	0.7321
673	7.2266	0.00086	9.8669	0.00083	446.25	0.187	0.7324
698	7.2296	0.00086	9.8730	0.00083	446.90	0.187	0.7323
723	7.2339	0.00086	9.8731	0.00083	447.43	0.187	0.7327

Table 2. Measured lattice parameters and volumes for γ-LaOF at 298 K, and from 723 K to 948 K.

| Temperature (K)	a (Å)	Uncertainty	c (Å)	Uncertainty	V (Å³)	Uncertainty
298	4.0798	0.00041	5.798	0.0020	96.51	0.118
723	4.1242	0.00045	5.855	0.0030	99.59	0.130
748	4.1192	0.00041	5.873	0.0020	99.65	0.119
773	4.1192	0.00041	5.873	0.0020	99.65	0.119
798	4.1213	0.00042	5.862	0.0020	99.57	0.119
823	4.1230	0.00042	5.862	0.0020	99.64	0.119
848	4.1246	0.00042	5.867	0.0020	99.80	0.119
873	4.1276	0.00042	5.864	0.0020	99.91	0.119
898	4.1293	0.00042	5.860	0.0020	99.92	0.119
923	4.1286	0.00050	5.866	0.0022	99.99	0.122
948	4.1311	0.00042	5.859	0.0020	100.00	0.119

Table 3. Measured lattice parameters and volumes for α-LaOF from 973 K to 1173 K.

| Temperature (K)	a (Å)	Uncertainty	V (Å³)	Uncertainty
298	5.756 *	0.003*	190.71*	
973	5.8424	0.00049	199.42	0.138
998	5.8443	0.00049	199.62	0.138
1023	5.8476	0.00050	199.95	0.138
1048	5.8489	0.00050	200.08	0.138
1073	5.8500	0.00050	200.20	0.138
1098	5.8526	0.00050	200.47	0.138
1123	5.8538	0.00050	200.60	0.138
1148	5.8531	0.00050	200.52	0.138
1173	5.8511	0.00050	200.32	0.138

*values for ambient temperature (298 K) from [22], because this structure was not recoverable to room temperature by quenching in the XRK-900 reactor stage.
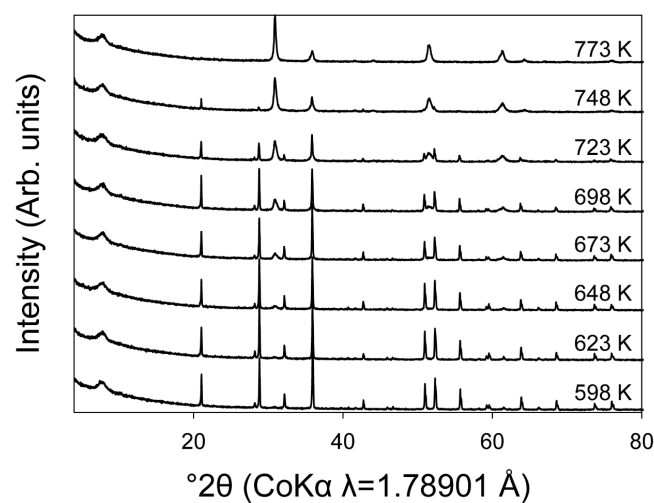
Figure 5. High temperature powder X-ray diffraction patterns from 598 K to 723 K. Bottom pattern is 598 K, and the patterns go up in 25° temperature increments. Bottom-most pattern exhibits only bastnäsite-(La). Top-most pattern exhibits only γ-LaOF. The middle six patterns exhibit both species as the decomposition reaction progresses from bastnäsite-(La) to γ-LaOF.
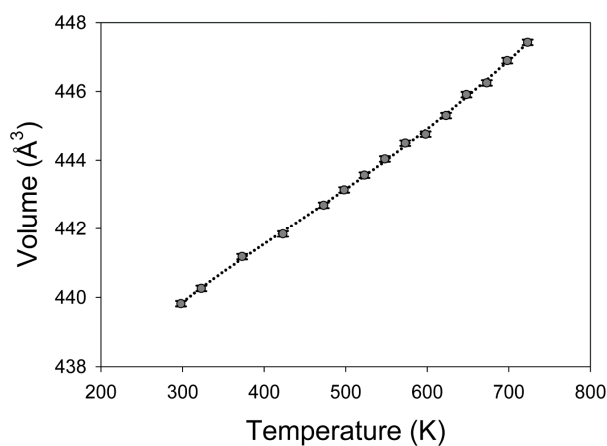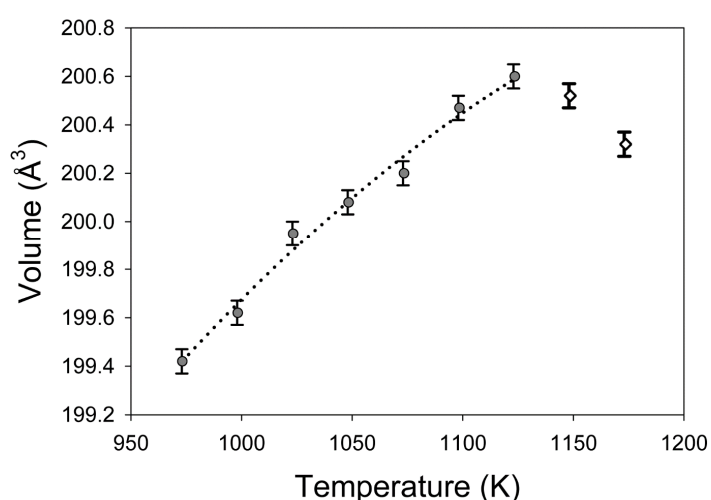

Figure 6. Measured unit cell volumes for bastnäsite-(La), as a function of temperature from 298 K to 723 K. The dotted black line is the fit for the Fei thermal equation of state [40].
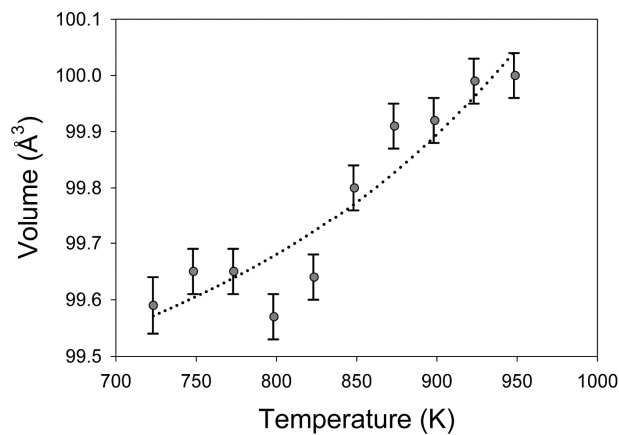
Figure 7. Measured unit cell volumes for tetragonal γ-LaOF as a function of temperature from 723 K to 948 K. The dotted black line is the fit for the Fei thermal equation of state [40].

Figure 8. Measured unit cell volumes for cubic α-LaOF as a function of temperature from 973 K to 1123 K. Gray-filled circles represent data used to fit the thermal equation of state in this temperature range. White diamonds represent temperature points 1148 K and 1173 K, which are above the temperature that coincides with a contraction in unit cell volume and an exotherm on the DSC curve. The dotted black line is the fit for the Fei thermal equation of state [40].

3.3. Single Crystal X-Ray Diffraction

At ambient temperature, 16 X-ray diffraction patterns of bastnäsite-(La) were collected from ambient pressure to 11.3 GPa. Over this pressure range, the *a-* crystallographic axis contracts from 7.187 Å to 6.974 Å, and the *c-* crystallographic axis contracts from 9.830 Å to 9.593 Å, with a corresponding unit cell volume contraction from 439.82 Å^3 to 404.06 Å^3. Table 4 lists the measured lattice parameters, calculated unit cell volumes, and crystallographic axis ratios for each pressure point. The unit cell volume data were fit to a third order Birch–Murnaghan equation of state [31,41] with $V_o = 439.82$ Å^3, $K_o = 105$ GPa, and $K' = 5.58$. Figure 9 illustrates the unit cell volume measurements superimposed over the calculated equation of state.
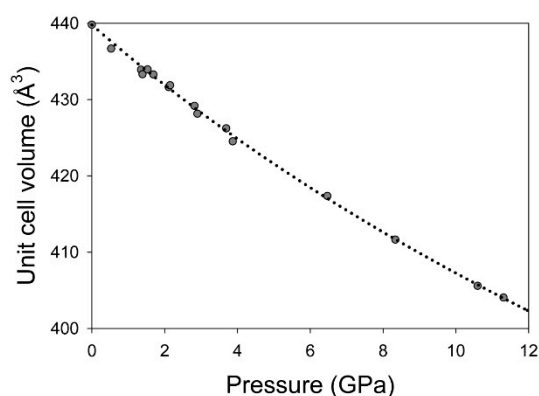
Figure 9. Pressure-volume data measured for bastnäsite-(La) fit to the 3rd order Birch–Murnaghan equation of state [41]. $V_0 = 439.82$ Å^3, $K_0 = 105$ GPa, $K' = 5.58$. Gray circles are measured volumes from Table 4, and dotted line represents equation of state fit to data.

Over the temperature range of 347 K to 673 K, nine X-ray diffraction patterns were collected between 4.9 GPa and 7.7 GPa. Over this range of conditions, the *a-* crystallographic axis varies between 7.057 Å and 7.086 Å, and the *c-* crystallographic axis varies between 9.730 Å and 9.685 Å, with corresponding variation in unit cell volumes between 423.11 Å^3 and 418.32 Å^3. Table 5 lists the

measured lattice parameters, calculated unit cell volumes, and crystallographic axis ratios for each pressure and temperature point.

Table 4. Bastnäsite-(La) measured lattice parameters, unit cell volumes, *a*/*c* crystallographic axis ratios, pressure transmitting media, and pressure standards from 0 GPa to 11.3 GPa at ambient temperature.

Pressure (GPa)	*a* (Å)	Uncertainty	*c* (Å)	Uncertainty	V (Å³)	Uncertainty	*a*/*c* Ratio	Pressure Media	Pressure Standard
0.00	7.187	0.002	9.833	0.040	439.82	0.044	0.7309	n/a	n/a
0.53	7.169	0.003	9.811	0.003	436.68	0.009	0.7307	Ne	Au
1.35	7.148	0.003	9.806	0.003	433.91	0.008	0.7289	Ne	Au
1.39	7.159	0.001	9.763	0.003	433.32	0.006	0.7333	He	Cu
1.53	7.158	0.001	9.780	0.003	433.96	0.006	0.7319	He	Cu
1.69	7.150	0.002	9.787	0.004	433.30	0.008	0.7306	He	Cu
2.11	7.144	0.004	9.766	0.006	431.64	0.013	0.7315	Ne	Au
2.15	7.145	0.001	9.769	0.003	431.88	0.005	0.7314	He	Cu
2.82	7.129	0.001	9.751	0.003	429.18	0.005	0.7311	He	Cu
2.90	7.117	0.002	9.761	0.002	428.15	0.006	0.7291	Ne	Au
3.69	7.111	0.001	9.734	0.002	426.23	0.004	0.7305	He	Cu
3.87	7.095	0.003	9.738	0.003	424.53	0.009	0.7286	Ne	Au
6.47	7.051	0.003	9.694	0.003	417.38	0.009	0.7274	Ne	Au
8.34	7.014	0.003	9.663	0.003	411.65	0.009	0.7259	Ne	Au
10.60	6.973	0.003	9.632	0.003	405.59	0.009	0.7239	Ne	Au
11.31	6.974	0.004	9.593	0.003	404.06	0.011	0.7270	Ne	Au

Table 5. Bastnäsite-(La) measured lattice parameters, unit cell volumes, and *a*/*c* crystallographic axis ratios from 4.9 GPa to 7.7 GPa pressure and from 347 K to 673 K temperature.

Pressure (GPa)	Temp (K)	*a* (Å)	Uncertainty	*c* (Å)	Uncertainty	V (Å³)	Uncertainty	*a*/*c* Ratio
4.9	347	7.086	0.001	9.730	0.002	423.11	0.005	0.7283
5.1	324	7.084	0.002	9.721	0.002	422.47	0.006	0.7287
5.8	373	7.076	0.002	9.696	0.002	420.44	0.006	0.7298
6.5	423	7.070	0.002	9.699	0.003	419.85	0.007	0.7289
6.7	473	7.060	0.002	9.691	0.002	418.32	0.006	0.7285
6.7	523	7.063	0.002	9.697	0.003	418.93	0.007	0.7284
7.0	573	7.057	0.002	9.713	0.003	418.91	0.007	0.7266
7.3	623	7.065	0.001	9.694	0.002	419.01	0.005	0.7288
7.7	673	7.064	0.002	9.685	0.002	418.53	0.006	0.7294

4. Discussion

From TGA/DSC and high temperature powder XRD data, it is apparent that at ambient pressure, the decarbonation temperature of bastnäsite-(La) is about 598 K. Above this temperature, the decomposition reaction of bastnäsite-(La) into γ-LaOF and CO_2 begins. Since our experiments were conducted without controlled pCO_2, this decarbonation point is not the equilibrium decomposition temperature; which at one bar pCO_2 is likely higher. The application of pressure significantly increases the stability of bastnäsite-(La), as was observed in our recrystallization experiments at 1073 K and 0.22 GPa (after five hours) and at 1123 K and 0.71 GPa after 21 h [28]. However, as these experiments were not reversed, a phase diagram for bastnäsite-(La) cannot yet be established. At 948 K, tetragonal γ-LaOF undergoes a first order structural phase transition reaction to cubic α-LaOF. The decomposition temperature for bastnäsite-(La) found in this study agrees with previous values reported by Janka and Schlied [15] who used similar methods, but did not report behavior for temperatures above 823 K. While the sample material cooled back down to 298 K, it transformed to γ-LaOF, the stable structure of lanthanum oxyfluoride at ambient conditions.

Table 6 lists the fitted thermal expansion coefficients for bastnäsite-(La), γ-LaOF, and α-LaOF over the temperature ranges measured in the high temperature powder X-ray diffraction experiments. Over the temperature ranges measured, all three species exhibit a trend of positive thermal expansion (Figures 6–8), except between 1123 K and 1173 K, where the α-LaOF unit cell

contracts. There is an endotherm in the DSC curve at 1123 K that could indicate a phase transition, but the X-ray diffraction patterns at these temperatures do not indicate a structural change, and the mass spectrometer did not detect any compounds outgassing at these temperatures; further studies are necessary to determine what this endotherm and coincident thermal contraction represent.

Table 6. Calculated thermal expansion coefficients for bastnäsite-(La), γ-LaOF, and α-LaOF.

Material	Dimension	Temp. Range (K)	α_{298} x 10^{-5}	a_0 x 10^{-5}	a_1 x 10^{-7}	a_2
bastnäsite-(La)	$a(a_0 = 7.1867$ Å$)$	298–723	1.73	−1.08	0.373	1.502
	$c(c_0 = 9.8328$ Å$)$	298–723	0.951	0.247	0.116	0.319
	V($V_0 = 439.82$ Å^3)	298–723	4.32	−1.68	0.834	3.126
γ-LaOF	$a(a_0 = 4.0798$ Å$)$	723–948	13.5	−17.9	1.90	22.879
	$c(c_0 = 5.798$ Å$)$	723–948	0.179	0.1785	−0.229	8.154
	V($V_0 = 96.51$ Å^3)	723–948	29.5	−24.1	2.42	41.147
α-LaOF	$a(a_0 = 5.756$ Å$)$	973–1123	−0.844	8.46	−0.625	−6.606
	V($V_0 = 190.71$ Å^3)	973–1123	−1.12	23.6	−1.73	−17.362

Note: Reference temperature for all fits is 298 K.

Thermal analysis has not been performed on any other fluorocarbonate minerals, so a direct comparison of the properties of bastnäsite-(La) measured in this investigation to other materials with similar structure is not possible. Others have investigated the thermal expansion of more common carbonates including aragonite ($CaCO_3$), strontianite ($SrCO_3$), cerrusite ($PbCO_3$), witherite ($BaCO_3$) [42], calcite ($CaCO_3$), and magnesite ($MgCO_3$) [43]. A comparison of the thermal equations of state for bastnäsite-(La) and these materials is given in Figure 10. Compared with these more common carbonates, bastnäsite-(La) experiences more thermal expansion for a given increase in temperature than the trigonal R-3c carbonates (calcite and magnesite), and less thermal expansion for a given increase in temperature than the orthorhombic Pmcn carbonates (aragonite, cerrusite, strontianite, and witherite). Additionally, as shown in Table 6, bastnäsite-(La)'s *a*- and *c*- crystallographic axes expand at different rates; all of the other carbonates listed above also exhibit some degree of anisotropic thermal expansion. Overall, this indicates that bastnäsite-(La)'s thermal expansion behavior is similar to that of other carbonate minerals.
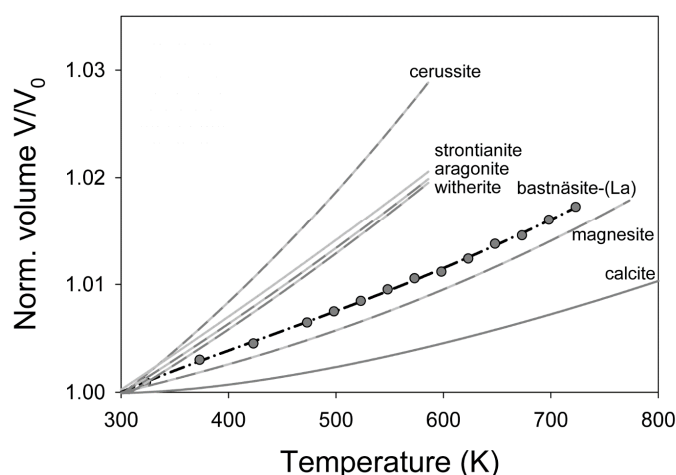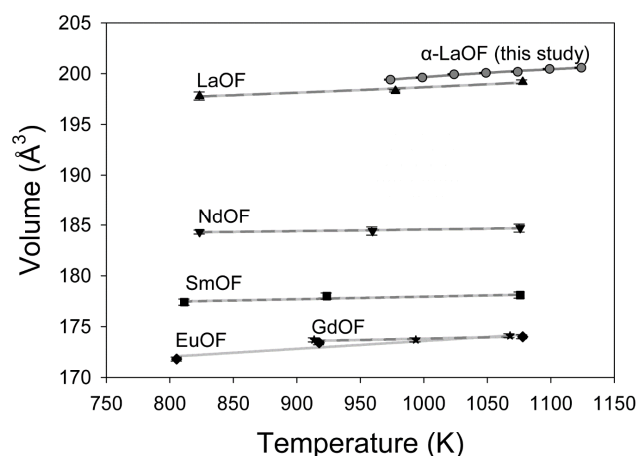

Figure 10. Comparisons of ambient pressure thermal equations of state for different carbonate minerals. Gray circles represent bastnäsite-(La) data from this study, and the dotted black line represent the fitted Fei equation of state [40] for bastnäsite-(La). Thermal equations of state are shown for calcite ($CaCO_3$), magnesite ($MgCO_3$) [43], witherite ($BaCO_3$), cerrusite ($PbCO_3$), strontianite ($SrCO_3$), and aragonite ($CaCO_3$) [42].

There are no previous studies of tetragonal REE-bearing oxyfluorides, but Achary et al. [24] synthesized the rhombohedral oxyfluorides of five REEs (La, Nd, Sm, Eu, and Gd), and used high temperature powder XRD to investigate their thermal expansion and phase transformation to cubic structures at high temperature. Their calculation and fitting of thermal expansion coefficients used the data for both rhombohedral and cubic phases, so the resulting thermal equations of state are not suitable to compare directly to that for α-LaOF derived in this study. However, using their data for just the cubic phases, we were able to fit thermal expansion coefficients using EOSFit7GUI [31]. Table 7 lists the fitted coefficients, and Figure 11 illustrates the thermal equations of state compared to that of α-LaOF measured in this study. The thermal expansion behavior we measured for α-LaOF is essentially the same as what we derived from Achary et al.'s data [24].

Table 7. Calculated thermal expansion coefficients for cubic REE-oxyfluorides.

Material	Temp. Range (K)	V_o (Å³)	α_{298} x 10^{-5}	a_0 x 10^{-5}	a_1 x 10^{-7}	a_2
α-LaOF †	973–1123	190.71	−1.12	23.6	−1.73	−17.362
α-LaOF *	823–1077	196.1	0.855	0.0017	0.286	0.0001
NdOF *	823–1075	183.8	0.268	0.0007	0.0895	0.0001
SmOF *	811–1075	176.2	1.4	1.4	0.00028	0
EuOF *	815–1077	168.2	4.49	4.49	0.00052	0.0001
GdOF *	913–1067	172.6	0.461	0.0044	0.1530	0

Note: Reference temperature for all fits is 298 K; † this study; * data from Achary, et. al [24].


Figure 11. Comparisons of ambient pressure thermal equations of state for cubic REE-OF compounds from this study and using data from Achary et al. [24] (solid symbols). Gray circles are data for cubic α-LaOF from this study.

The anisotropy of bastnäsite-(La) is enhanced under compression; the *a*- crystallographic axis contracts more than the *c*- crystallographic axis. The changing ratio of *a/c* is given in Table 4. Similarly, the *a*- crystallographic axis is also more expansive during heating (Table 1). As illustrated in Figure 1, the planar carbonate ions are arranged in the structure such that they lie on planes containing the *c*- crystallographic axis. Others [44–46] have observed rigid body behavior of CO_3^{2-} anions in other carbonates at high pressure. Thus, we suggest that most of the expansion and contraction of the structure is accommodated by the La-O and La-F bonds.

There are no compressibility data fit to equations of state or any bulk moduli measured from other methods (e.g., ultrasonic methods) in the literature for bastnäsite or any other fluorocarbonate minerals, so a direct comparison of the properties of bastnäsite-(La) measured in this investigation to materials with similar structure is not possible. However, our results are consistent with recent work on natural materials that shows that the bastnäsite structure is stable up to 25 GPa at room temperature [47]. Anderson and Nafe [48] found that when comparing many compounds' bulk

moduli versus their specific ionic volumes, multiple trends emerged. Figure 12 displays their data, with additional data for carbonate minerals from Knittle [49], Merlini [50], and Xu [51]. Anderson and Nafe [48] identified a sulfide-selenide-telluride trend, an oxide trend, a fluorite trend, and an alkali-halide trend. Rhodochrosite, dolomite, ankerite, calcite, strontianite, and witherite form a separate carbonate trend (yellow line in Figure 12), but the hydroxycarbonates azurite and malachite do not lie on this trend. The values measured for bastnäsite-(La) in this study plot in a location consistent with the carbonate trend, the fluorite trend, as well as the oxide trend. Work on other fluorocarbonates needs to be completed in order to determine which of these trends bastnäsites follow, or if fluorocarbonates have a separate trend. If the speculation above that bastnäsite-(La)'s compressional anisotropy is related to rigid body behavior and orientation of the carbonate ions is correct, it is then likely that bastnäsites would follow the carbonate trend.
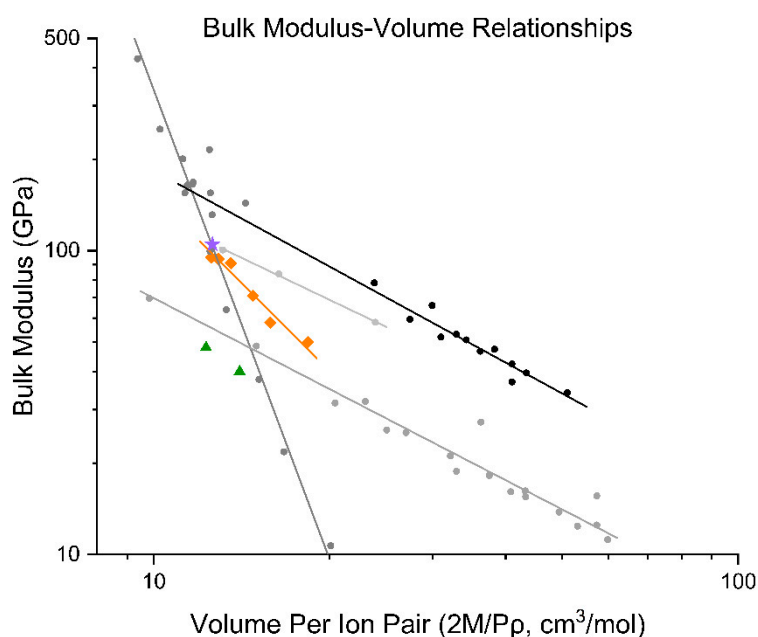
Figure 12. Bulk modulus versus specific volume for simple oxides, alkali halides, fluorites, sulfides, selenides, tellurides, and carbonates. Small circles include data from [48] and [49]. Large purple star is the value for bastnäsite-(La) measured in this study ($2M/P\rho$ = 12.60 cm^3/mol, K_o = 105 GPa), large orange diamonds are carbonates from [49], and green triangles are malachite and azurite from [50,51]. Dark gray line is the oxide trend, black line is the sulfide, selenide, and telluride trend, light gray line is the fluorite trend, medium gray line is the alkali-halide trend, and orange line is proposed carbonate trend.

While some of our measurements were taken at elevated temperature and pressure (Table 5), there is not enough data to properly fit a high temperature and pressure equation of state. However, these data can be used to evaluate whether our isothermal and thermal equations of state can be combined to predict bastnäsite-(La)'s unit cell volume at high temperature and pressure. Thus, for each pressure temperature point measured in our heated DAC experiments, we calculated the value for V_o (at P = 0) using our values for the thermal equation of state [40], and then used our Birch–Murnaghan equation of state [41] to calculate the pressure required to produce the observed unit cell volume. The pressures calculated in this way agree well with those measured from the copper pressure standard. Table 8 lists the measured temperatures, unit cell volumes, and pressures, and the calculated pressures. Since the temperatures and volumes from the elevated temperature DAC experiments were not used in the fitting of Fei's thermal equation of state or in the fitting of the Birch–Murnaghan equation of state, these data show that the combination of both equations is a reasonable

approximation for modeling changes in volume due to both pressure and temperature simultaneously.

Table 8. List of heated DAC experiments comparing measured pressure using the Cu standard versus calculated pressures using the Fei thermal EOS [40] parameters. Difference is calculated by subtracting the measured pressure from the calculated pressure. Error is calculated by dividing the difference by the measured pressure.

Temp (K)	V (Å³)	Measured P (GPa)	Calculated P (GPa)	Difference	Error
347	423.11	4.90	5.03	0.13	0.03
324	422.47	5.09	5.11	0.02	0.00
373	420.44	5.78	6.02	0.24	0.04
423	419.85	6.46	6.46	0.00	0.00
473	418.32	6.74	7.23	0.49	0.07
523	418.93	6.71	7.28	0.57	0.08
573	418.91	6.97	7.57	0.60	0.09
623	419.01	7.33	7.84	0.51	0.07
673	418.53	7.69	8.33	0.64	0.08

5. Conclusions

Compressibility, thermal expansion and phase stability are fundamental thermodynamic properties of materials, and as such are significant in understanding how they interact with the geologic settings in which the minerals naturally occur. Bastnäsite-La and the lanthanum oxyfluoride polymorphs addressed above are important REE-bearing compounds, and thus studying them is useful for understanding how REE bearing compounds form and participate in chemical reactions with other compounds. Additionally, since bastnäsite is found in carbonatites, it is an important mineral to investigate in order to understand carbonated magmas and the formation of carbonatite-related ore deposits. Gaining insight into the thermodynamic behavior of bastnäsite and other fluorocarbonates could potentially lead to better methods of locating and processing REE ore in the future.

References

1. Chen, Z. Global rare earth resources and scenarios of future rare earth industry. *J. Rare Earths* **2011**, *29*, 1–6.
2. Long, K.R.; Van Gosen, B.S.; Foley, N.K.; Cordier, D. The Principal Rare Earth Elements Deposits of the United States: A Summary of Domestic Deposits and a Global Perspective. *US Geol. Surv. Sci. Investig.* **2010**, *2010*, 96.
3. Workman, R.K.; Hart, S.R. Major and trace element composition of the depleted MORB mantle (DMM). *Earth Planet. Sci. Lett.* **2005**, *231*, 53–72.
4. Ni, Y.; Hughes, J.M.; Mariano, A.N. The atomic arrangement of bastnäsite-(Ce), Ce(CO$_3$)F, and structural elements of synchysite-(Ce), röntgenite-(Ce), and parisite-(Ce). *Am. Mineral.* **1993**, *78*, 415–418.
5. Olson, J.C.; Shawe, D.R.; Pray, L.C.; Sharp, W.N.; Hewett, D.F. Rare-Earth Mineral Deposits of the Mountain Pass District San Bernardino County California. *Geol. Surv. Prof. Pap.* **1954**, *261*, 4–15.
6. Williams-Jones, A.E.; Wood, S.A. A preliminary petrogenetic grid for REE fluorocarbonates and associated minerals. *Geochim. Cosmochim. Acta* **1992**, *56*, 725–738.
7. Hsu, L.C. Synthesis and Stability of Bastnaesites in a Part of the System (Ce,La)-F-H-C-O. *Mineral. Petrol.* **1992**, *47*, 87–101.
8. Schmandt, D.S.; Cook, N.J.; Ciobanu, C.L.; Ehrig, K.; Wade, B.P.; Gilbert, S.; Kamenetsky, V.S. Rare earth element fluorocarbonate minerals from the olympic dam Cu-U-Au-Ag deposit, South Australia. *Minerals* **2017**, *7*, 202.
9. Oftedal, I. Zur Kristallstruktur von Bastnäsit, (Ce,La)FCO$_3$. *Zeitschrift fur Krist. Krist. Krist. Krist.* **1931**, *78*, 462.
10. Donnay, G.; Donnay, J.D.H. The Crystallography of Bastnaesite, Parisite, Roentgenite, and Synchisite. *Am. Mineral.* **1953**, *38*, 932–963.
11. Castor, S.B. Rare Earth Deposits of North America. *Resour. Geol.* **2008**, *58*, 337–347.
12. Castor, S.B. The Mountain Pass Rare-Earth Carbonatite and Associated Ultrapotassic Rocks, California. *Can. Mineral.* **2008**, *46*, 779–806.
13. Shivaramaiah, R.; Anderko, A.; Riman, R.E.; Navrotsky, A. Thermodynamics of bastnaesite: A major rare earth ore mineral. *Am. Mineral.* **2016**, *101*, 1129–1134.
14. Gysi, A.P.; Williams-Jones, A.E. The thermodynamic properties of bastnäsite-(Ce) and parisite-(Ce). *Chem. Geol.* **2015**, *392*, 87–101.
15. Janka, O.; Schleid, T. Facile Synthesis of Bastnaesite-Type LaF[CO$_3$] and Its Thermal Decomposition to LaOF for Bulk and Eu^{3+}-Doped Samples. *Eur. J. Inorg. Chem.* **2009**, *2009*, 357–362.
16. Woo, D.C.; Lee, M.-H.; Jung, W.-S. Synthesis and characterization of rhombohedral- and tetragonal-lanthanum oxyfluoride powders. *Ceram. Int.* **2013**, *39*, 1533–1538.
17. Jacob, K.T.; Saji, V.S.; Waseda, Y. Lanthanum Oxyfluoride: Structure, Stability, and Ionic Conductivity. *Int. J. Appl. Ceram. Technol.* **2006**, *3*, 312–321.
18. Fergus, J.W.; Chen, H.-P. Structure and Conductivity of Tetragonal and Rhombohedral Lanthanum Oxyfluoride Compounds. *J. Electrochem. Soc.* **2000**, *147*, 4696–4704.
19. Shinn, D.B.; Eick, H.A. Phase Analyses of Lanthanide Oxide Fluorides. *Inorg. Chem.* **1969**, *8*, 232–235.
20. Zachariasen, W.H. Crystal Chemical Studies of the 5f-series of Elements. XIV. Oxyfluorides, XOF. *Acta Crystallogr.* **1951**, *4*, 231–236.
21. Pistorius, C.W.F.T. Effect of Pressure on the Rhombohedral/Cubic Transitions of Some Lanthanide Oxide Fluorides. *J. Less-Common Met.* **1973**, *31*, 119–124.
22. Klemm, V.W.; Klein, H.-A. Lanthanoxyfluorid [Lanthanum Oxyfluoride]. *Zeitschrift fur Anorg. und Allg. Chemie (in Germany).* **1941**, *248*, 167–171.
23. Mathews, M.D.; Tyagi, A.K.; Moorthy, P.N. Study of phase transition in REOF system by dilatometry (RE = La, Nd, Sm, Gd, Eu and Y). *Thermochim. Acta* **1997**, *298*, 165–167.
24. Achary, S.N.; Ambekar, B.R.; Mathews, M.D.; Tyagi, A.K.; Moorthy, P.N. Study of phase transition and volume thermal expansion in a rare-earth (RE) oxyfluoride system by high-temperature XRD (RE = La, Nd, Sm, Eu and Gd). *Thermochim. Acta* **1998**, *320*, 239–243.
25. Holtstam, D.; Grins, J.; Nysten, P. Håleniusite- (La) from the Bastnäs Deposit, Västmandland, Sweden: A new REE Oxyfluoride Mineral Species. *Can. Mineral.* **2004**, *42*, 1097–1103.
26. Momma, K.; Izumi, F. VESTA 3 for three-dimensional visualization of crystal, volumetric and

morphology data. *J. Appl. Crystallogr.* **2011**, *44*, 1272–1276.

27. Tullis, T.E.; Tullis, J. Experimental Rock Deformation Techniques. *Geophys. Monogr.* 1986, *36*, 297–324.

28. Rowland II, R.L. Phase Equilibria, Compressibility, and Thermal Analysis of Bastnaesite-(La), University of Nevada, Las Vegas, 2017.

29. Altomare, A.; Corriero, N.; Cuocci, C.; Falcicchio, A.; Moliterni, A.; Rizzi, R. QUALX2.0: A qualitative phase analysis software using the freely available database POW_COD. *J. Appl. Crystallogr.* **2015**, *48*, 598–603.

30. Holland, T.J.B.; Redfern, S.A.T. Unit cell refinement from powder diffraction data: the use of regression diagnostics. *Mineral. Mag.* **1997**, *61*, 65–77.

31. Angel, R.J.; Gonzalez-Platas, J.; Alvaro, M. EosFit7c and a Fortran module (library) for equation of state calculations. *Zeitschrift fur Krist.* **2014**, *229*, 405–419.

32. Kantor, I.; Prakapenka, V.; Kantor, A.; Dera, P.; Kurnosov, A.; Sinogeikin, S.; Dubrovinskaia, N.; Dubrovinsky, L. BX90: A new diamond anvil cell design for X-ray diffraction and optical measurements. *Rev. Sci. Instrum.* **2012**, *83*.

33. Hrubiak, R.; Sinogeikin, S.; Rod, E.; Shen, G. The laser micro-machining system for diamond anvil cell experiments and general precision machining applications at the High Pressure Collaborative Access Team. *Rev. Sci. Instrum.* **2015**, *86*.

34. Rivers, M.; Prakapenka, V.B.; Kubo, A.; Pullins, C.; Holl, C.M.; Jacobsen, S.D. The COMPRES/GSECARS gas-loading system for diamond anvil cells at the Advanced Photon Source. *High Press. Res.* **2008**, *28*, 273–292.

35. Mao, H.K.; Xu, J.; Bell, P.M. Calibration of the Ruby Pressure Gauge to 800 kbar Under Quasi-Hydrostatic Conditions. *J. Geophys. Res.* **1986**, *91*, 4673.

36. Hirose, K.; Sata, N.; Komabayashi, T.; Ohishi, Y. Simultaneous volume measurements of Au and MgO to 140 GPa and thermal equation of state of Au based on the MgO pressure scale. *Phys. Earth Planet. Inter.* **2008**, *167*, 149–154.

37. Wang, Y.; Zhang, J.; Xu, H.; Lin, Z.; Daemen, L.L.; Zhao, Y.; Wang, L. Thermal equation of state of copper studied by high P-T synchrotron x-ray diffraction. *Appl. Phys. Lett.* **2009**, *94*, 4.

38. Hammersley, A.P. FIT2D: A multi-purpose data reduction, analysis and visualization program. *J. Appl. Crystallogr.* **2016**, *49*, 646–652.

39. Dera, P.; Zhuravlev, K.; Prakapenka, V.; Rivers, M.L.; Finkelstein, G.J.; Grubor-Urosevic, O.; Tschauner, O.; Clark, S.M.; Downs, R.T. High pressure single-crystal micro X-ray diffraction analysis with GSE_ADA/RSV software. *High Press. Res.* **2013**, *33*, 466–484.

40. Fei, Y. Thermal Expansion. In *Mineral Physics and Crystallography: A Handbook of Physical Constants*; Ahrens, T.J., Ed.; American Geophysical Union: Washington, DC, USA, 1995; pp. 29–44, ISBN 0-87590-852-7.

41. Birch, F. Finite Elastic Strain of Cubic Crystals. *Phys. Rev.* **1947**, *71*, 809–824.

42. Ye, Y.; Smyth, J.R.; Boni, P. Crystal structure and thermal expansion of aragonite-group carbonates by single-crystal X-ray diffraction. *Am. Mineral.* **2012**, *97*, 707–712.

43. Markgraf, S.A.; Reeder, R.J. High-temperature structure refinements of calcite and magnesite. *Am. Mineral.* **1985**, *70*, 590–600.

44. Ross, N.L.; Reeder, R.J. High-pressure structural study of dolomite and ankerite. *Am. Mineral.* **1992**, *77*, 412–421.

45. Ross, N.L. The equation of state and high-pressure behavior of magnesite. *Am. Mineral.* **1997**, *82*, 682–688.

46. Zhang, J.; Reeder, R.J. Comparative compressibilities of calcite-structure carbonates: Deviations from empirical relations. *Am. Mineral.* **1999**, *84*, 861–870.

47. Vennari, C.E.; Williams, Q. High-pressure Raman and Nd^{3+} luminescence spectroscopy of bastnäsite-$(REE)CO_3F$. *Am. Mineral.* **2019**, *104*, 1389–1401.

48. Anderson, O.L.; Nafe, J.E. The Bulk Modulus-Volume Relationship for Oxide Compounds and Related Geophysical Problems. *J. Geophys. Res.* **1965**, *70*, 3951–3963.

49. Knittle, E. Static Compression Measurements of Equation of State. In *Mineral physics and Crystallography: A Handbook of Physical Constants*; Ahrens, T.A., Ed.; American Geophysical Union: Washington, DC, USA, 1995; pp. 98–142.

50. Merlini, M.; Perchiazzi, N.; Hanfland, M.; Bossak, A. Phase transition at high pressure in $Cu_2CO_3(OH)_2$

related to the reduction of the Jahn–Teller effect. *Acta Crystallogr. Sect. B Struct. Sci.* **2012**, *B68*, 266–274.

51. Xu, J.; Kuang, Y.; Zhang, B.; Liu, Y.; Fan, D.; Zhou, W.; Xie, H. High-pressure study of azurite $Cu_3(CO_3)_2(OH)_2$ by synchrotron radiation X-ray diffraction and Raman spectroscopy. *Phys. Chem. Miner.* **2015**, *42*, 805–816.